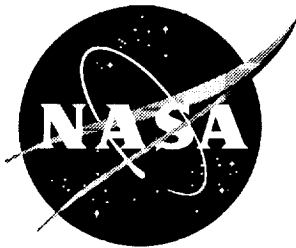


NASA/CR-1998-208967



# Numerical Study of Turbulence Model Predictions for the MD 30P/30N and NHLP-2D Three-Element Highlift Configurations

*Joseph H. Morrison*  
*Analytical Services & Materials, Inc., Hampton, Virginia*

National Aeronautics and  
Space Administration

Langley Research Center  
Hampton, Virginia 23681-2199

Prepared for Langley Research Center  
under Contract NAS1-96014

---

December 1998

---

Available from:

NASA Center for AeroSpace Information (CASI)  
7121 Standard Drive  
Hanover, MD 21076-1320  
(301) 621-0390

National Technical Information Service (NTIS)  
5285 Port Royal Road  
Springfield, VA 22161-2171  
(703) 605-6000

---

## Abstract

This report details calculations for the McDonnell-Douglas 30P/30N and the NHLP-2D three-element highlift configurations. Calculations were performed with the Reynolds averaged Navier-Stokes code ISAAC to study the effects of various numerical issues on high lift predictions. These issues include the effect of numerical accuracy on the advection terms of the turbulence equations, Navier-Stokes versus the thin-layer Navier-Stokes approximation, an alternative formulation of the production term, and the performance of several turbulence models. The effect of the transition location on the NHLP-2D flow solution was investigated. Two empirical transition models were used to estimate the transition location.



# 1 Introduction

The prediction of high lift configurations consisting of multiple airfoil elements remains a challenge to computational fluid dynamics (CFD). Multi-element airfoils contain a wide variety of flow physics which must be accurately modeled. Each airfoil element has a stagnation point and boundary layers developing in pressure gradients. The boundary layers develop along a curved surface and may transition from laminar to turbulent flow. Additionally, the wake of each element eventually merges with the boundary layer from subsequent elements. However, optimum high lift multiple element designs are generally achieved when the slat wake is kept distinct from the main element boundary layer for the greatest distance on the main element.

The flow around the slat is quite complex. The slat windward surface is highly curved with large flow acceleration. The flow at the slat trailing edge can be laminar, transitional, or turbulent. The slat leeward surface is highly concave. The leeward flow must accelerate through the slat-main element gap around a very sharp bend. The flow often separates due to the slat geometry, reattaching near the slat trailing edge. The free shear layer developed at the recirculation boundary is most likely turbulent. The wake developing at the trailing edge of the slat is then created from the laminar, transitional, or turbulent upper surface flow and the turbulent lower surface flow. Additionally, the flow around the lower surface may be unsteady.

Therefore, the predictive capability for high lift multiple element airfoil configurations is dependent on the ability to accurately model i) boundary layer transition on a curved surface in a strong pressure gradient ii) turbulent boundary layer development on a curved surface in a strong pressure gradient iii) transitional and turbulent wake development iv) separating and reattaching flow and v) wind tunnel effects.

Rumsey et al.[1] demonstrated the need to include the transition location and wind tunnel walls to accurately predict multiple element airfoil flows. They studied the McDonnell Douglas MD-30P/30N three-element highlift configuration that was tested in the NASA Langley LTPT wind tunnel [2],[3],[4] and the NHLP-2D airfoil proposed as an AGARD test case [5] and used as a test case for the CFD Society of Canada [6]. Rumsey et al.[1] provided experimentally measured transition location on all three elements of the MD-30P/30N airfoil. The NHLP-2D airfoil had the transition specified on the main element through the addition of a transition strip on the upper and lower surfaces; transition occurred naturally on the slat and flap.

The current study examines the same two configurations as Rumsey et al.[1]. The purpose of this work is to investigate several numerical issues of the solution procedure on these configurations, specifically, grid convergence, first versus second order differencing of the advection operator in the turbulence model, the form of the turbulence production term, and full Navier-Stokes versus thin-layer differencing. The effect of transition specification for the NHLP-2D airfoil is also investigated.

## 2 Technical Approach

Calculations are presented with a farfield vortex boundary condition[7]. Results from Rumsey et al.[1] show that including the wind tunnel walls in the calculation improves the comparison with wind tunnel data. The purpose of these calculations is to investigate various numerical and modeling effects; the use of the farfield vortex boundary condition results in faster convergence and fewer computer hours required.

### 2.1 Flow Solver

The ISAAC code [8] solves the two or three dimensional Navier-Stokes equations using the MUSCL upwinding procedure with Roe's flux difference splitting for the mean flow equations coupled to turbulence model equations. Viscous terms are discretized using second-order central differences in either the thin-layer or full Navier-Stokes form. The temporal integration is accomplished with an implicit, diagonalized, approximate factorization scheme. Multigrid acceleration is applied to the mean flow equations and mesh sequencing (full multigrid) is used to provide an initial solution.

The velocity and heat flux were set to zero on the airfoil surface. Viscous terms were calculated in both grid coordinate directions.

### 2.2 Turbulence Models

The following three turbulence models were used in this study; Wilcox's  $K$ - $\omega$  eddy viscosity model [9], the Speziale-Abid-Anderson  $K$ - $\varepsilon$  eddy viscosity model[13], and an algebraic stress model [14]. The turbulence model equations are given below in Cartesian tensor notation. Favre averaging is applied to the flow variables, where  $\rho$  is the density,  $u_k$  are the Cartesian velocity components,  $p$  is the pressure,  $K$  is the turbulent kinetic energy,  $\varepsilon$  is the dissipation rate,  $\omega$  is the specific dissipation rate,  $\mu$  is the molecular viscosity, and  $\mu_t$  is the turbulent eddy viscosity.

#### 2.2.1 $K$ - $\omega$ Eddy-Viscosity Turbulence Model

The  $K$ - $\omega$  turbulence model was developed by Wilcox[9] and applied to a variety of flows. The model is unique in that it requires no wall damping terms to be integrated to the wall. The  $K$ - $\omega$  model requires the integration of the  $K$  and  $\omega$  transport equations:

$$\frac{\partial}{\partial t}(\rho K) + \frac{\partial}{\partial x_k}(\rho u_k K) = \rho \mathcal{P} - C_{K2} \rho \omega K + \frac{\partial}{\partial x_k} \left[ \left( \mu + \frac{\mu_t}{\sigma_K} \right) \frac{\partial K}{\partial x_j} \right] \quad (1)$$

$$\frac{\partial}{\partial t}(\rho \omega) + \frac{\partial}{\partial x_k}(\rho u_k \omega) = C_{\omega 1} \frac{\rho \omega}{K} \mathcal{P} - C_{\omega 2} \rho \omega^2 + \frac{\partial}{\partial x_k} \left[ \left( \mu + \frac{\mu_t}{\sigma_\omega} \right) \frac{\partial \omega}{\partial x_j} \right] \quad (2)$$

with the eddy viscosity calculated as

$$\mu_t = C_\mu \frac{\rho K}{\omega} \quad (3)$$

the production is given as

$$\rho \mathcal{P} = -\rho \tau_{ij} \frac{\partial u_i}{\partial x_j} \quad (4)$$

## 2.2 Turbulence Models

and the model coefficients are given in Table 1.

| $C_\mu$ | $C_{K2}$ | $C_{\omega1}$ | $C_{\omega2}$ | $\sigma_K$ | $\sigma_\omega$ |
|---------|----------|---------------|---------------|------------|-----------------|
| 1.0     | 0.09     | 5/9           | 3/40          | 2.0        | 2.0             |

Table 1: Constants for the  $K$ - $\omega$  model.

The Reynolds stresses are modeled with the linear Boussinesq assumption

$$-\rho\tau_{ij} = \mu_t \left[ \left( \frac{\partial u_i}{\partial x_j} + \frac{\partial u_j}{\partial x_i} \right) - \frac{2}{3} \frac{\partial u_k}{\partial x_k} \delta_{ij} \right] - \frac{2}{3} \rho K \delta_{ij} \quad (5)$$

### 2.2.2 SAA $K$ - $\varepsilon$ Eddy-Viscosity Turbulence Model

The Speziale-Abid-Anderson (SAA)  $K$ - $\varepsilon$  model[13] may be written as

$$\frac{\partial}{\partial t}(\rho K) + \frac{\partial}{\partial x_k}(\rho u_k K) = \rho \mathcal{P} - \rho \varepsilon + \frac{\partial}{\partial x_k} \left[ \left( \mu + \frac{\mu_t}{\sigma_K} \right) \frac{\partial K}{\partial x_j} \right] \quad (6)$$

$$\frac{\partial}{\partial t}(\rho \varepsilon) + \frac{\partial}{\partial x_k}(\rho u_k \varepsilon) = C_{\varepsilon 1} \frac{\rho \varepsilon}{K} \mathcal{P} - C_{\varepsilon 2} f_2 \frac{\rho \varepsilon^2}{K} + \frac{\partial}{\partial x_k} \left[ \left( \mu + \frac{\mu_t}{\sigma_\varepsilon} \right) \frac{\partial \varepsilon}{\partial x_j} \right] \quad (7)$$

where the eddy viscosity is calculated as

$$\mu_t = C_\mu f_\mu \frac{\rho K^2}{\varepsilon} \quad (8)$$

and the Boussinesq approximation, Eq. 5, is applied for the Reynolds stresses. The damping functions are given as

$$f_\mu = \left( 1 + 3.45/\sqrt{Re_t} \right) \tanh(y^+/70) \quad (9)$$

$$f_2 = \left[ 1 - \frac{2}{9} \exp(-Re_t^2/36) \right] [1 - \exp(-y^+/4.9)]^2 \quad (10)$$

where  $Re_t = \rho K^2/\mu \varepsilon$  is the turbulence Reynolds number and  $y^+ = \rho y u_\tau/\mu$ ,  $u_\tau = \sqrt{\tau_w/\rho}$ . The SAA model coefficients are given in Table 2.

| $C_\mu$ | $C_{\varepsilon 1}$ | $C_{\varepsilon 2}$ | $\sigma_K$ | $\sigma_\varepsilon$ |
|---------|---------------------|---------------------|------------|----------------------|
| 0.09    | 1.44                | 1.83                | 1.0        | 1.36                 |

Table 2: Constants for the SAA  $K$ - $\varepsilon$  model.

### 2.2.3 Algebraic Stress Turbulence Model

The algebraic stress model (ASM)[14] replaces the linear Boussinesq stress-strain relationship with the following non-linear form:

$$-\rho\tau_{ij} = 2\mu_t^* \left[ \left( S_{ij} - \frac{1}{3} S_{kk} \delta_{ij} \right) + \alpha_4 \frac{K}{\varepsilon} (S_{ik} W_{kj} + S_{jk} W_{ki}) - \alpha_5 \frac{K}{\varepsilon} \left( S_{ik} S_{kj} - \frac{1}{3} S_{kl} S_{kl} \delta_{ij} \right) \right] - \frac{2}{3} \rho K \delta_{ij} \quad (11)$$

## 2.2 Turbulence Models

---

where

$$\mu_i^* = \alpha_1 \frac{3(1 + \eta^2) + 0.2(\eta^6 + \xi^6)}{3 + \eta^2 + 6\eta^2\xi^2 + 6\xi^2 + \eta^6 + \xi^6} \quad (12)$$

the strain rate tensor and the rotation tensor are given as

$$S_{ij} = \frac{1}{2} \left( \frac{\partial u_i}{\partial x_j} + \frac{\partial u_j}{\partial x_i} \right) \quad (13)$$

$$W_{ij} = \frac{1}{2} \left( \frac{\partial u_i}{\partial x_j} - \frac{\partial u_j}{\partial x_i} \right) \quad (14)$$

and the constants are given as:

$$\begin{aligned} \alpha_1 &= \left( \frac{4}{3} - C_2 \right) g/2 & \alpha_2 &= (2 - C_3)^2 g^2/4 & \alpha_3 &= (2 - C_4)^2 g^2/4 \\ \alpha_4 &= (2 - C_4) g/2 & \alpha_5 &= (2 - C_3) g & g &= \frac{1}{(C_1/2) + C_5 - 1} \end{aligned} \quad (15)$$

The coefficients from the SSG [10] pressure-strain correlation are  $C_1 = 6.8$ ,  $C_2 = 0.36$ ,  $C_3 = 1.25$ ,  $C_4 = 0.40$ , and  $C_5 = 1.88$ .

The  $K$  transport equation (Eq. 6) and the  $\varepsilon$  transport equation (Eq. 7) are solved with the damping function

$$f_2 = \{1 - \exp[-(y^+/5.5)]\}^2 \quad (16)$$

and the coefficients given in Table 3.

| $C_\mu$ | $C_{\varepsilon 1}$ | $C_{\varepsilon 2}$ | $\sigma_K$ | $\sigma_\varepsilon$ |
|---------|---------------------|---------------------|------------|----------------------|
| 0.081   | 1.44                | 1.83                | 1.0        | 1.51                 |

Table 3: Constants for ASM model.

### 2.2.4 CFL3D Algebraic Stress Turbulence Model

The CFL3D ASM model[15] is the same form as the ASM model, but has the following damping function

$$f_2 = \{1 - \exp[-(Re_k/12)]\} \quad (17)$$

where

$$Re_k = \frac{\rho \sqrt{K} y}{\mu} \quad (18)$$

and the coefficients are given in Table 4.

| $C_\mu$ | $C_{\varepsilon 1}$ | $C_{\varepsilon 2}$ | $\sigma_K$ | $\sigma_\varepsilon$ |
|---------|---------------------|---------------------|------------|----------------------|
| 0.081   | 1.376               | 1.83                | 1.0        | 1.3                  |

Table 4: Constants for CFL3D ASM model.

## 2.3 Transition Specification

---

### 2.3 Transition Specification

Transition is specified by setting the turbulence production (Eq. 4) to zero in a prescribed region. This results in laminar flow in the prescribed region and is equivalent to forcing transition. Transition requires the external specification of the transition location.

## 3 Results

### 3.1 MD 30P/30N

The flow conditions for the test case are given in Table 5. Transition locations are specified from the work of Rumsey et al.[1].

|            |                   |
|------------|-------------------|
| $M_\infty$ | 0.2               |
| $Re$       | $9.0 \times 10^6$ |
| $\alpha$   | $19^\circ$        |
| $T_\infty$ | $460^\circ R$     |

Table 5: Flow parameters for 30P/30N three-element airfoil.

Figure 1 shows the locations of the experimental velocity profiles. The first measurement location is on the main element; no detailed measurements are available on the slat to compare with model predictions.

The grid [1] consists of four C-grids: the first block is a  $745 \times 57$  C-grid around the slat, the second block is a  $597 \times 89$  C-grid around the main element, the third block is a  $265 \times 65$  C-grid around the flap, and the fourth block is a  $685 \times 33$  C-grid around all of the other grids. Additionally, a coarser mesh that is formed by deleting every other grid point in both coordinate directions is used to study grid convergence. The first grid point off the airfoil surface for the fine grid was located such that  $y^+ < 0.65$ . There were at least 25 grid points in the boundary layers.

#### 3.1.1 The Effect of Numerical Accuracy on Turbulence Models

This section documents the effect of first order versus second order accurate discretization of the advection terms in the turbulence model equations on both the coarse and fine grids.

Turbulence model equations for complex flows can exhibit stiffness, non-positive behavior, and be difficult to converge. To alleviate some of the stiffness, ensure positivity, and improve the robustness of the solution procedure, it is often assumed that a first order upwind discretization of the advection terms on the turbulence transport equations is sufficient.

Figure 2 shows the pressure calculated with the first order and the second order advection for the  $K$  and  $\omega$  turbulence equations[9] on the fine mesh and the mesh coarsened once by removing every other grid point in both coordinate directions with the experimental data from Paschal et al. [3]. The first and second order results are identical to plotting accuracy on both the fine and coarse mesh; the order of the advection operator makes no discernible difference in the calculated wall pressure. However, the fine grid increases the suction level on the suction side of the slat. Both grids give reasonable predictions of the surface pressure on all three elements.

Figures 3-5 show the velocity profiles calculated with the first and second order advection for the  $K$  and  $\omega$  turbulence equations. The fine grid calculations show an increased wake deficit from the coarse grid calculations. The velocity profile at  $x/c = 0.45$  shown in Figure 3 demonstrates less merging of the slat wake with the main element boundary layer for the

second order advection operator for the turbulence equations. The second order advection shows a clear boundary layer on the main element and a separate slat wake. The first order advection smears the edge of the slat wake down into the outer edge of the main element boundary layer.

The second order advection also predicts a higher edge velocity for the main element and flap boundary layers for  $x/c \geq 0.85$  as shown in Figures 4 and 5. The flap trailing edge boundary layer ( $x/c = 1.1125$ ) edge velocity is underpredicted by the first order advection on both grids and only approaches the experimental value for the fine grid with the second order advection.

Neither the first nor the second order advection calculations demonstrate grid convergence on this sequence of meshes. The first and second order solutions should coincide on a sufficiently fine mesh with the second order solution achieving grid convergence more rapidly than the first order solution. The results show that the improved grid resolution increases the wake defect. Additionally, the first order advection on the turbulence equations smears out the wake deficit.

#### 3.1.2 The Effect of Viscous Terms on Model Predictions

Figure 6 shows velocity profiles on the main element and the flap calculated with the thin-layer approximation and with full Navier-Stokes terms. The calculation with the full Navier-Stokes terms shows a slight difference at the slat wake edge. There is almost no change in the calculation in the boundary layer of the main element or in the wake of the main element with the full Navier-Stokes terms. The level of changes introduced with the full Navier-Stokes terms as compared to the thin-layer approximation is small. This is a result of the good level of grid orthogonality in the shear layers.

#### 3.1.3 The Effect of Production Term on Model Predictions

Menter[12] noted that calculations without a specified transition location resulted in very high eddy viscosities outside the boundary layer in the region of the stagnation point. The production in this region is given as the difference in the normal stresses times a velocity gradient and is modeled in an eddy viscosity model as a positive term. To overcome the unphysical production of turbulence, he suggested that turbulence production, Eq. 4, can be approximated for two-dimensional airfoil flows in the following manner:

$$\rho\mathcal{P} = \mu_t\Omega^2 \tag{19}$$

where

$$\Omega = \sqrt{2W_{ij}W_{ij}} \tag{20}$$

is the magnitude of the vorticity.

The production term, Eq. 4, is an exact term in the derived turbulent kinetic energy transport equation. Any errors in the form of this term come from the stress-strain relationship that is applied. Algebraic stress models improve on the stress-strain relationship used in eddy viscosity models. In the current work, the unphysical high eddy viscosity in the stagnation region is controlled by specifying a transition location.

Figures 7-9 show the velocity profiles calculated with the  $K$ - $\omega$  turbulence model[9] with the alternate production term. The solution at the first station,  $x/c = 0.1075$ , shows minimal difference between the two solutions for the two forms of the production term. The main element boundary layer and the slat wake are almost identical. Further downstream differences begin to appear. By the  $x/c = 0.45$  location, the vorticity based production calculates a fuller and thicker boundary layer than the exact production term. The vorticity based production also calculates a smaller wake defect for the slat wake than the exact production term calculates. The results on the flap show smaller wake defects for both the slat wake and the main element wake with the vorticity based production and more merging of the wakes. The exact production predictions are closer to the experimental data for the main element wake, but the vorticity based production predictions are closer to the experiment for the slat wake. The vorticity based production predicts an increased maximum edge velocity at the flap middle and trailing edge than the exact production term predicts. The increased edge velocity is closer to the experimental data.

#### 3.1.4 The Effect of Damping Functions on the Algebraic Stress Model

Figure 10 plots the damping functions for the ASM model, Eq. 16, and the CFL3D ASM model, Eq. 17, for a log layer. Both damping functions are  $\mathcal{O}(y^2)$  to remove the singularity in the destruction of dissipation term. The CFL3D ASM damping function turn off at  $y^+ \approx 15$  while the ASM damping function damps much further into the log layer to  $y^+ \approx 35$ . Additionally, damping based on  $y^+$  is ill-posed for separated flows; the damping extends even further into the computational domain as the wall shear stress is zero at the separation and reattachment points resulting in small values of  $y^+$  at large distances from the wall.

Figures 11-13 show the velocity profiles calculated with the ASM model and the CFL3D ASM model. The profiles at the first location,  $x/c = 0.1075$ , show minimal differences between the ASM and the CFL3D ASM models. However, by the  $x/c = 0.45$  station the two models are showing noticeable differences; the CFL3D ASM model predicts a thicker main element boundary layer and a wider wake. Additionally, the CFL3D ASM model predicts the wake further from the surface than the ASM model. These trends continue on all profiles to the trailing edge of the flap. The CFL3D ASM model predicts more merging of the wakes with the boundary layers and a lower peak velocity in the merging region. On the flap, the CFL3D ASM model shows improved comparison with experiment as the wake deficit is predicted smaller than the ASM model and the peak velocity at the merged boundary layer/wake is lower.

#### 3.1.5 The Effect of Turbulence Models on the Flow Field

Figures 14-16 show the velocity profiles calculated with the Speziale-Abid-Anderson (SAA)  $K$ - $\epsilon$  model[13], the algebraic stress model (ASM)[14], and the  $K$ - $\omega$  turbulence model[9]. All three of the models overpredict the slat wake defect for all of the measuring stations. At the first station,  $x/c = 0.1075$ , the ASM model predicts the lowest edge velocity of the three models for the main element boundary layer and the  $K$ - $\omega$  model predicts the edge velocity closest to the experiment. Accounting for the different edge velocities for the models, all three models appear to predict a very similar wake defect and wake width for the slat. Further downstream,  $x/c \geq 0.45$ , the  $K$ - $\omega$  model predicts more spreading of the slat wake.

### 3.2 NHLP-2D

---

The  $K-\omega$  model also predicts the slat wake closer to the airfoil surface than the SAA model, and the ASM model predicts the slat wake furthest from the surface. At  $x/c = 0.45$  and  $0.85$  the  $K-\omega$  model predicts a fuller and thicker main element boundary layer than the SAA model and the ASM model underpredicts the boundary layer.

The  $K-\omega$  model underpredicts the main element wake at the  $x/c \geq 0.89817$  locations, but predicts about the correct level of minimum velocity at the  $x/c = 1.1125$  location. At all three locations the  $K-\omega$  model predicts the main element wake too close to the surface. The  $K-\omega$  model underpredicts the edge velocity of the flap boundary layer and does not predict the main element wake development well.

The ASM model overpredicts the main element wake defect and wake width. The ASM model does the best job of predicting the flap boundary layer edge velocity at the trailing edge, but it had underpredicted the flap boundary layer at the flap leading edge. The ASM model does the best job of predicting the location of the wakes, but consistently overpredicts the wake defect and spreading.

The SAA model best predicts the main element wake defect and wake width of the three models. The location of the wakes is predicted too close to the surface by the SAA model. The flap boundary layer is predicted best by the SAA model.

Rumsey et al. [1] showed that the calculations including the wind tunnel walls improved the locations of the wakes and the agreement with experimental data. The current calculations were performed using an unbounded boundary condition. A transition model should be included to model the effect of the physical transition process.

### 3.2 NHLP-2D

The flow conditions for the NHLP-2D test case are given in Table 6. The experimental transition was specified at 12.5% chord on the upper and lower surfaces of the main element. The slat and flap were not tripped and the transition locations were not experimentally measured.

|            |                    |
|------------|--------------------|
| $M_\infty$ | 0.195              |
| $Re$       | $3.52 \times 10^6$ |
| $\alpha$   | $4.01^\circ$       |

Table 6: Flow parameters for NHLP-2D three-element airfoil.

Figure 17 shows the locations of the experimental profiles of total pressure coefficient. The first measurement location is on the main element; no detailed measurements are available on the slat to compare with model predictions.

The grid [6] consists of four C-grids: the first block is a  $245 \times 49$  C-grid around the flap, the second block is a  $549 \times 89$  C-grid around the main element, the third block is a  $577 \times 57$  C-grid around the slat, and the fourth block is a  $641 \times 33$  C-grid around all of the other grids. The grid employs one-to-one point connectivity at the zonal interfaces. The outer boundary is approximately 10 chords from the body. The first grid point off the airfoil surface for the fine grid was located such that  $y^+ < 0.62$ , except for a small region on the slat where  $y^+ \approx 1.1$ . There were at least 20 grid points in the boundary layer.

### 3.2.1 Free Transition Calculations

The first set of calculations were performed with the main element tripped at 12.5% chord as specified in the experiment; the slat and flap transition occurred where the turbulence model calculated. It is important to note that none of the turbulence models is calibrated to predict transition. Figure 18 shows the surface pressure calculated with the  $K-\omega$  model, the SAA model, and the ASM model. All of the models show good agreement with the experimental values of wall pressure.

Figure 19 shows profiles of the total pressure coefficient at four different stations on the main element and the flap. The plot at  $x/c = 0.35$  shows the slat wake and the boundary layer on the main element. All three of the models predict too large of a defect for the slat wake. The experimental data is very sparse in the region of the slat wake, but appears to show a very narrow and weak wake. All of the models predict a stronger wake that is displaced further from the main element surface than the experimental data indicates. Additionally, all of the models predict a larger edge velocity for the main element boundary layer than the experiment indicates. The experiment shows more merging of the slat wake and main element boundary layer than the calculations show. There are differences in the various models, but they all fundamentally show a more distinct wake and boundary layer than the experiment.

The experimental profiles at all of the other downstream locations confirm the merging of the slat wake with the main element boundary layer; the slat wake is completely missing from the experimental total pressure profiles at the  $x/c = 0.91$  and higher locations. All three of the models predict a distinct slat wake in the outer edge of the main element boundary layer all the way to the flap trailing edge ( $x/c = 1.214$ ). The algebraic Reynolds stress model shows the smallest wake at all of the stations and the  $K-\omega$  model shows the largest wake at all of the locations. The wake location is predicted very similarly for all three models, but the wake defect and wake width vary.

Rumsey et al.[1] demonstrated that specification of transition on the slat had a major impact on the calculation of multi-element airfoils. Therefore, the transition location predicted by each of the models was calculated. The transition location was determined from the flow solution as the location where the turbulent eddy-viscosity exceeded the molecular viscosity across (the majority of) the boundary layer. Figure 20 shows the calculated location of the transition point on the slat for all three models. The  $K-\omega$  model predicts transition closest to the stagnation point on both the upper and lower surfaces of the slat. The ASM model predicts transition at the most aft location. The delay in the transition reduces the initial boundary layer thickness at the slat trailing edge and reduces the initial wake width and wake defect. This accounts for part of the variation in the slat wake predictions in the profiles shown previously.

Figure 21 shows the calculated location of the transition point on the flap for all three models. For the flap, the ASM model predicts transition closest to the stagnation point, and substantially upstream of the other models, on the upper surface. The  $K-\omega$  model predicts an earlier transition on the flap lower surface and the ASM and SAA models predict the same transition location on the lower surface. The effect of the early transition on the ASM model is clearly evident on the flap boundary layer at the  $x/c = 1.214$  location with a much reduced total pressure (velocity) near the surface.

It is important to reiterate that none of these models is derived and calibrated to predict transition. All of the models will have a transition behavior as turbulence levels grow, but this behavior is not calibrated to match physical transition.

### 3.2.2 Specified Transition Calculations

To investigate the issue of slat transition, the calculations were repeated with the transition location on the slat set to the trailing edge of the slat on the upper surface and to the corner of the cove region on the lower surface. The flow on the windward portion of the slat was calculated as laminar flow and the flow in the cove region was calculated as turbulent flow. The main element transition was maintained at 12.5% chord on the upper and lower surface and the flap was left as free transition.

Figure 22 shows the total pressure coefficient profiles at the four measurement locations calculated with the  $K$ - $\omega$  model with free transition and with transition on the slat fixed as detailed above. The results at  $x/c = 0.35$  show a slight reduction in the wake defect, a decrease in the wake width, and a slight shift of the wake towards the main element surface. All of these trends are closer to the experimental results. The wake defect and width show greater changes in the downstream profiles and the wake continues to move closer to the surface. Changes in the slat wake also change the wake flow of the main element over the flap as is evident in the  $x/c = 1.066$  and  $x/c = 1.214$  profiles.

Figure 23 shows the wall pressure for all three models with the transition location specified on the slat. The wall pressure shows minimal improvement over the results with free transition that were shown in Figure 18.

Figure 24 shows the profiles of the total pressure coefficient for all three models with the transition location specified on the slat. All three of the models show a reduced wake defect and narrower wake at all four stations for the transition fixed on the slat as compared to the free transition case.

Figure 25 shows the calculation with the  $K$ - $\omega$  model using both first and second order accurate differencing on the advection terms in the turbulence transport equations (advection terms in the mean equations and viscous terms in all equations are second order accurate for all calculations). The  $\epsilon$  based models (SAA and ASM) required the use of first order advection on the turbulence models to achieve a solution. The second order solution is also shown for the grid coarsened one level by deleting every other grid line in both coordinate directions.

The first order turbulence advection calculation shows a much smaller wake deficit and more merging with the boundary layer than the second order calculation. This trend is visible at all four streamwise locations. The first order solution also shows a smaller peak total pressure at the edge of the boundary layer at the flap trailing edge. The second order solution on the coarse grid shows very poor comparison to experiment and shows merging of the slat wake with the boundary layer much earlier than the fine grid results. The coarse grid results also provide a poor prediction of the main element boundary layer. The solutions are not grid converged and further grid refinement is necessary to verify the wake defect and wake width discrepancies.

### 3.2.3 Slat Transition Prediction

Several empirical procedures have been developed to predict transition locations. Michel[16] (as reported in White[17]) developed a correlation that transition of incompressible flow about airfoils occurs when the Reynolds number based on the momentum thickness

$$Re_{\theta_i} = \frac{\rho_e U_e \theta_i}{\mu_e} \quad (21)$$

satisfies

$$Re_{\theta_i} \approx 2.9 Re_s^{0.4} \quad (22)$$

where  $Re_s$  is the Reynolds number based on  $s$ , the distance along the surface from the stagnation point,

$$Re_s = \frac{\rho_e U_e s}{\mu_e} \quad (23)$$

and the subscript,  $e$ , denotes the boundary layer edge conditions. This correlation is for incompressible flows, therefore the transformation of Mann and Whitten (see e.g. White[17]) is used to relate the compressible momentum thickness to the incompressible momentum thickness [18]

$$\theta = \theta_i \left( \frac{T_0}{T_e} \right)^3 \quad (24)$$

where  $T_0$  is the total temperature, the compressible momentum thickness is calculated as

$$\theta = \int_0^\delta \frac{\rho U}{\rho_e U_e} \left( 1 - \frac{U}{U_e} \right) dy \quad (25)$$

and  $\delta$  is the boundary layer thickness. Transition is calculated to occur at the first  $s$  location where Eq. 22 is satisfied.

Figure 26 shows the value of the momentum thickness Reynolds number for the upper surface of the slat calculated assuming laminar flow. The calculated value of  $Re_{\theta_i}$  never exceeds Michel's correlation for transition. Therefore, transition is not predicted on the slat surface by Michel's correlation.

Wazzan et al.[19] developed the  $H-Re_x$  correlation for transition based on the  $e^9$  method. They demonstrated that a wide range of transition data, including the effects of pressure gradient, suction, and (low rates of) heat transfer, collapsed to a single curve when  $Re_x$  was plotted as a function of the incompressible shape factor,  $H_i$ , where the compressible shape factor is defined as

$$H = \delta^* / \theta \quad (26)$$

the displacement thickness is given as

$$\delta^* = \int_0^\delta \left( 1 - \frac{\rho U}{\rho_e U_e} \right) dy \quad (27)$$

and the incompressible shape factor is taken from the Mann and Whitten transformation [17]

$$H = H_i \left( \frac{T_{aw}}{T_0} \right) \left( 1 + \frac{\gamma - 1}{2} M_e^2 \right) + \frac{\gamma - 1}{2} M_e^2 \quad (28)$$

where  $T_{aw}$  is the adiabatic wall temperature and  $M_e$  is the Mach number at the boundary layer edge. Wazzan et al. provided a fit to the experimental curve as

$$\log(Re_x) = -40.4557 + 64.8066H_i - 26.7538H_i^2 + 3.3819H_i^3 \quad 2.1 < H_i < 2.8 \quad (29)$$

For general geometries,  $x$  is replaced with  $s$ , where  $s$  is the distance along the body measured from the stagnation point.

Figure 27 plots the curve from Eq. 29 along with the values from the flow calculation. The value of  $Re_s$  calculated from the flow solution never exceeds the value of  $Re_x$  required for transition by the  $H-Re_x$  correlation. Therefore, the  $H-Re_x$  correlation never predicts transition to occur on the slat upper surface.

Both Michel's correlation and the  $H-Re_x$  correlation predict that the slat upper surface remains laminar all the way to the trailing edge. Figure 22 demonstrated that the  $K-\omega$  model results were improved when the flow on the upper surface of the slat was assumed laminar. However, Figure 24 shows that discrepancies in the predictions remain quite large for all three of the models which predict a more distinct slat wake, too large of a wake deficit, and the slat wake located too far from the main element surface. The transition model that is applied in these calculations assumes instantaneous transition. The current calculations set the transition at the slat trailing edge which is consistent with the empirical transition correlations. However, the calculations transition to fully turbulent flow at the trailing edge while the experiment transitions over some distance.

The flow in the cove region of the slat is assumed turbulent; the experiment probably develops turbulence in this region quickly but there may be unsteady shedding of vortices from the slat corner and coherent structures interacting with the lower half of slat wake. The development of the slat near wake with a transition upper half and a turbulent lower half with large scale coherent structures in the pressure gradient with curvature is the key to improving the flow predictions. Unfortunately, the experiment provides insufficient data to analyze the slat near wake. The experiment would ideally provide a detailed mapping of this flow including unsteady measurements to identify whether or not coherent structures are important.

#### 3.2.4 Main Element Transition Trips

The boundary layer on the upper surface of the main element is tripped using an inset metal strip that is 0.125 inches wide and 0.009 inches high located at 12.5% chord. The laminar boundary layer thickness at the specified transition location is calculated to be,  $\delta_u = 0.03537$  inches. The trip height is  $h \approx .254\delta_u$  and the width is  $l \approx 3.53\delta_u$ . There will be a separated region in front of and a separated region behind the rectangular trip. This large of an obstruction in the boundary layer will result in an artificial thickening of the boundary layer that will persist far downstream. The  $x/c = 0.35$  measuring station is only  $191\delta_u$  downstream from the trip. The boundary layer at this location will not be the same as a fully developed boundary layer that began developing at the trip location - which is what is modeled in the calculations. The momentum defect from the trip could explain part of the total pressure defect near the wall at the  $x/c = 0.35$  location. The artificial thickening of the boundary layer would result in quicker merging of the slat wake with the main element boundary layer which is also seen in the data.

### 3.2 NHLP-2D

---

The boundary layer on the lower surface of the main element is tripped using plastic tape that is 0.125 inches wide and 0.012 inches high located at 12.5% chord. The laminar boundary layer thickness at the specified transition location is calculated to be,  $\delta_l = 0.03169$  inches. The trip height is  $h \approx .379\delta_l$  and the width is  $l \approx 3.94\delta_l$ . This trip is even more intrusive to the boundary layer than on the upper surface.

### 4 Concluding Remarks

The current calculations did not demonstrate grid independence for either highlift configuration with either the first or second order turbulence advection. Increased grid resolution and the second order turbulence advection increased the wake defect, decreased the wake width, and reduced the wake/boundary layer merging.

The results for the NHLP-2D with transition specified improved the calculated wake deficit and wake location. Two empirical transition prediction methods were used to justify the NHLP-2D slat transition locations. However, while the transition location was investigated and improved, the transition location and extent is not available from the experiment and is not modeled correctly, i.e. an instantaneous transition is specified on the slat rather than a transition region. Rumsey et al.[1] used experimental transition criteria for the MD 30P/30N three-element airfoil and improved the comparison with the data more than the current study achieved for the NHLP-2D airfoil. The developing wake from the slat upper and lower surfaces is not sufficiently well documented to answer fundamental modeling questions. Substantial questions as to transition and coherent large-scale structures remain in the slat cove region and near wake.

The experimental trips used on the NHLP-2D airfoil intruded a significant distance into the boundary layer and disturbed the boundary layer development. The tripped boundary layer development is not modeled with instantaneous transition. The calculations should be repeated including the trips in the geometry. The effects of the trip separation regions and the developing boundary layer could then be calculated.

The calculations with the thin-layer Navier-Stokes terms and the full Navier-Stokes terms showed minimal differences. This is mainly due to the high level of grid orthogonality in the shear layers.

The calculations with the production based on vorticity showed a smaller wake defect, poorer agreement with the boundary layer, and more merging of the wake and boundary layer than the exact production term.

Results for three different models were compared on the MD 30P/30N three-element highlift configuration. All of the models calculated too large of a wake defect. Grid resolved calculations including wall effects and an improved transition model are required to more accurately compare the models. The ASM models from ISAAC and CFL3D produced very similar results. The functional form of the damping function used in CFL3D is preferred in flows with separation and reattachment to prevent issues when the wall shear stress approaches zero.

Additional experimental data on the slat and in the slat near wake is necessary for both configurations to identify turbulence model deficiencies. The experimental data is also needed to answer whether the flow in the wake is unsteady due to shedding from the slat cove corner.

### Acknowledgements

The author wishes to thank A. Bertelrud of AS&M and C. L. Rumsey of NASA Langley for many insightful discussions of this work. The author also wishes to thank T. B. Gatski, K. M. Jones, and J. L. Thomas of NASA Langley for their support of this work.

References

- [1] Rumsey, C. L., Gatski, T. B., Ying, S. X., and Bertelrud, A., "Prediction of High-Lift Flows Using Turbulent Closure Models," *AIAA Journal*, Vol. 36, No. 5, May 1998.
- [2] Stainback, P. C., McGhee, R. J., Beasley, W. D., and Morgan, H. L. Jr., "The Langley Research Center's Low Turbulence Pressure Tunnel," AIAA Paper 86-0762, 1986.
- [3] Paschal, K., Goodman, W., McGhee, R., Walker, B., and Wilcox, P. A., "Evaluation of Tunnel Sidewall Boundary Layer Control Systems for High-Lift Airfoil Testing," AIAA Paper 91-3243, 1991.
- [4] Bertelrud, A., "Transition on a Three-Element High Lift Configuration at High Reynolds Numbers," AIAA Paper 98-0703, 1998.
- [5] Burt, M., "A Selection of Experimental Test Cases for the Validation of CFD Codes: Chapter 5 - Summaries of the Test Cases," AGARD AR-303, Vol. 1, August 1994.
- [6] Fejtek, I., "Summary of Code Validation Results for a Multiple Element Airfoil Test Case," AIAA Paper 97-1932, 1997.
- [7] Thomas, J. L. and Salas, M. D., "Far-Field Boundary Conditions for Transonic Lifting Solutions to the Euler Equations," *AIAA Journal*, Vol. 24, No. 7, July 1986.
- [8] Morrison, J. H., "A Compressible Navier-Stokes Solver with Two-Equation and Reynolds Stress Turbulence Closure Models," NASA CR-4440, May 1992.
- [9] Wilcox, D. C., "Reassessment of the Scale Determining Equation for Advanced Turbulence Models," *AIAA Journal*, Vol. 26, No. 11, November 1988.
- [10] Speziale, C. G., Sarkar, S. and Gatski, T. B., "Modeling the Pressure-Strain Correlation of Turbulence: An Invariant Dynamical Systems Approach," *J. Fluid Mech.*, Vol. 227, 1991, pp. 245-272.
- [11] Gatski, T. B. and Speziale, C. G., "On Explicit Algebraic Stress Models for Complex Turbulent Flows," *J. Fluid Mech.*, Vol. 254, 1993.
- [12] Menter, F. R., "Improved Two-Equation  $K-\omega$  Turbulence Models for Aerodynamic Flows," NASA TM 103975, Oct. 1992.
- [13] Speziale, C. G., Abid, R., and Anderson, C., "Critical Evaluation of Two-Equation Models for Near-Wall Turbulence," *AIAA Journal*, Vol. 30, No. 2, February 1992.
- [14] Abid, R., Morrison, J. H., Gatski, T. B., and Speziale, C. G., "Prediction of Aerodynamic Flows with a New Explicit Algebraic Stress Model," *AIAA Journal*, Vol. 34, No. 12, December 1996.
- [15] Krist, S. L., Biedron, R. T., and Rumsey, C. L., *CFL3D User's Manual (Version 5.0)*, NASA/TM-1998-208444, June 1998.

## REFERENCES

---

- [16] Michel, R., "Determination du Point de Transition Et Calcul de la Trainee des Profils d'Ailes en Incompressible," *La Recherche Aeronautique*, No. 24, 1951.
- [17] White, F. M., *Viscous Fluid Flow*, McGraw-Hill, 1974.
- [18] Bertelrud, A., Private Communication, 1998.
- [19] Wazzan, A. R., Gazley, C., and Smith, A. M. O., " $H-R_x$  Method for Predicting Transition," *AIAA Journal*, Vol. 19, No. 6, June 1981.

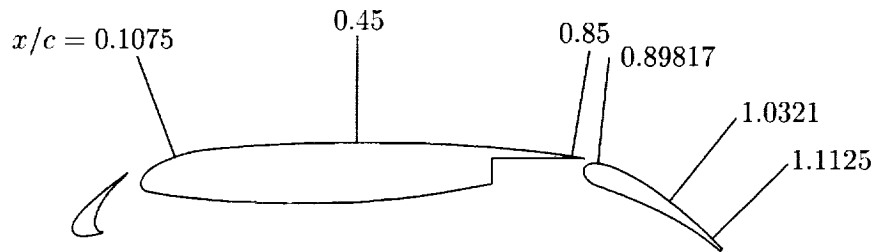


Figure 1: Location of velocity profiles for MD-30P/30N multi-element airfoil.

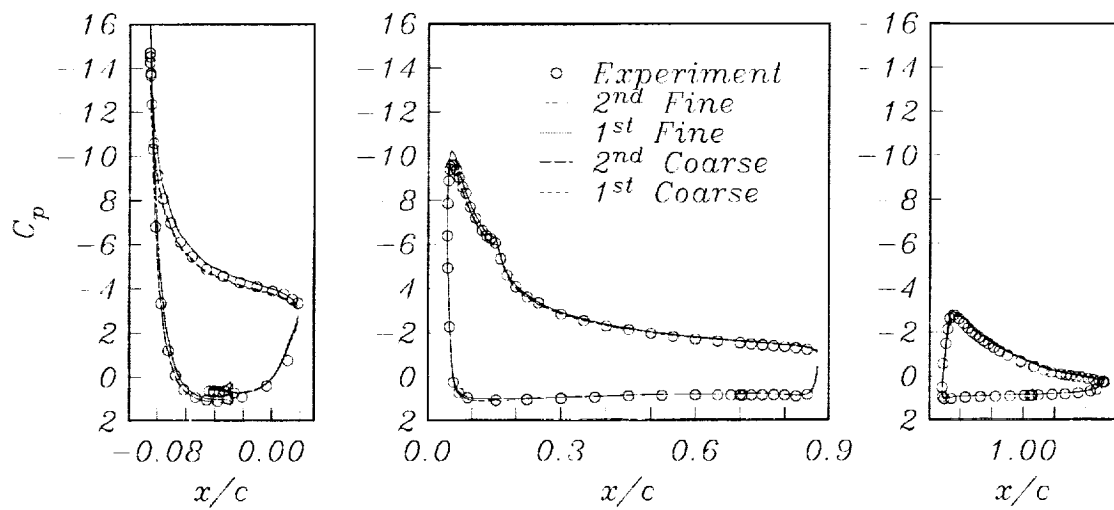


Figure 2: Wall pressure coefficient for MD-30P/30N multi-element airfoil calculated with 1<sup>st</sup> and 2<sup>nd</sup> order advection and  $K-\omega$  model.

Figures

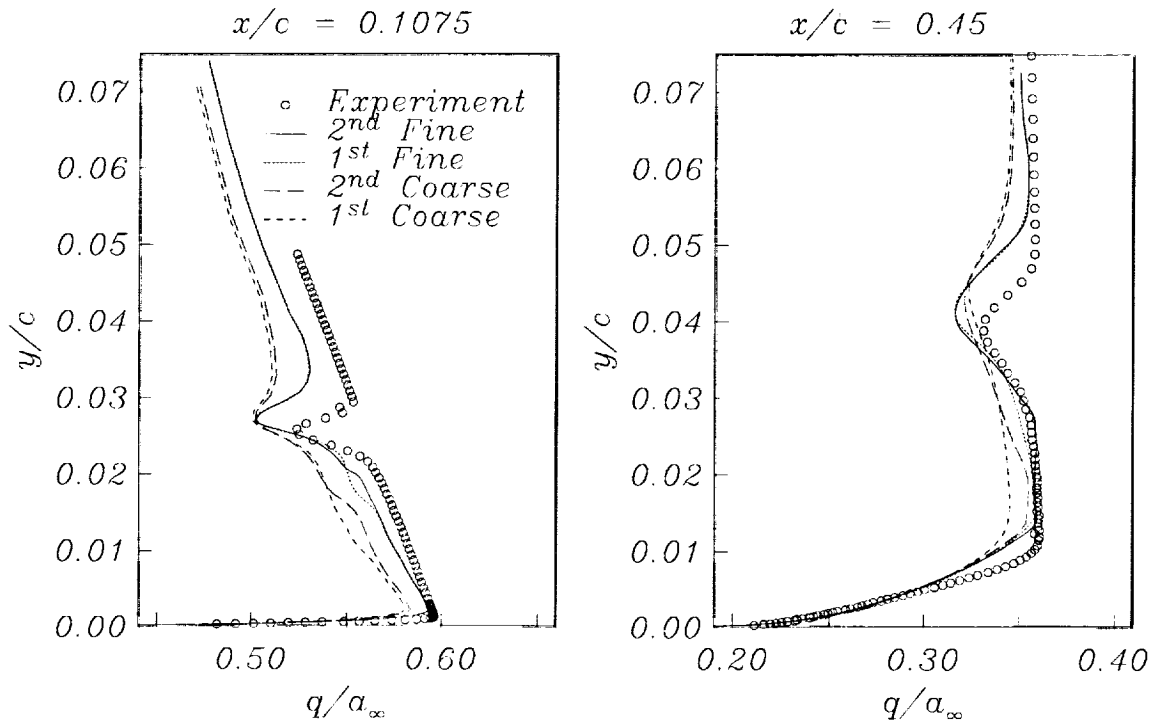


Figure 3: Velocity profiles on the MD-30P/30N main element calculated with 1<sup>st</sup> and 2<sup>nd</sup> order advection on the  $K$  and  $\omega$  equations.

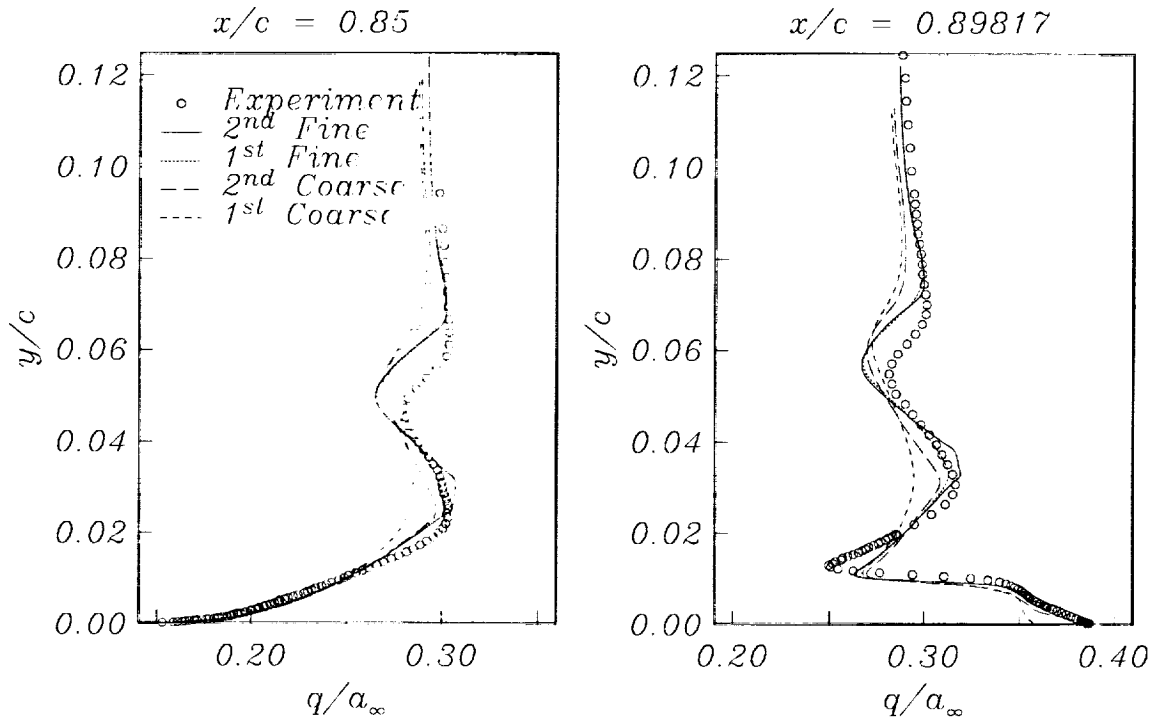


Figure 4: Velocity profiles at the MD-30P/30N main element-flap gap calculated with 1<sup>st</sup> and 2<sup>nd</sup> order advection on the  $K$  and  $\omega$  equations.

Figures

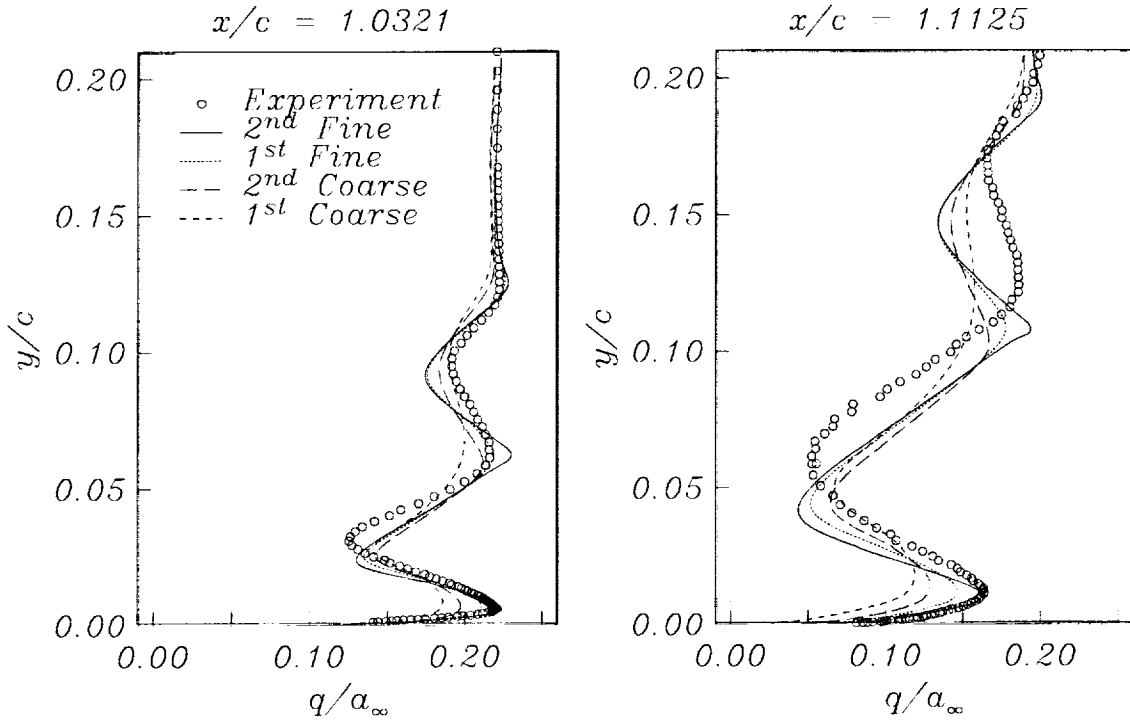


Figure 5: Velocity profiles on the MD-30P/30N flap calculated with 1<sup>st</sup> and 2<sup>nd</sup> order advection on the  $K$  and  $\omega$  equations.

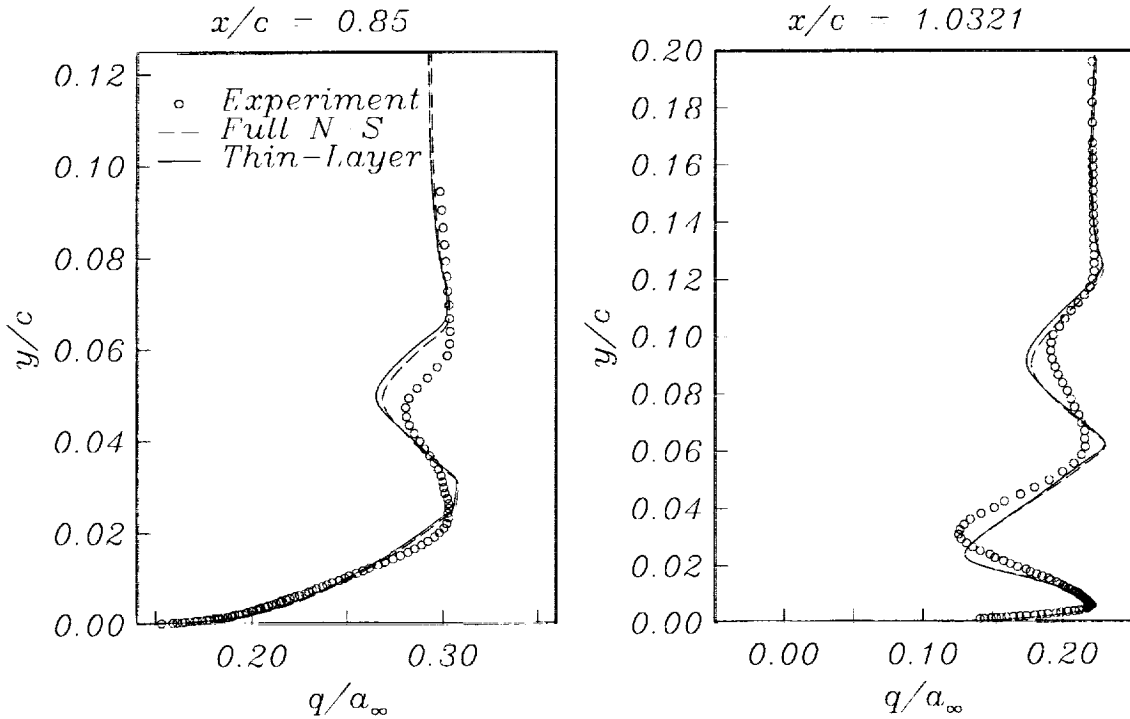


Figure 6: Velocity profiles on the MD-30P/30N main element and flap calculated with thin-layer approximation and full Navier-Stokes terms  $K$  and  $\omega$  equations.

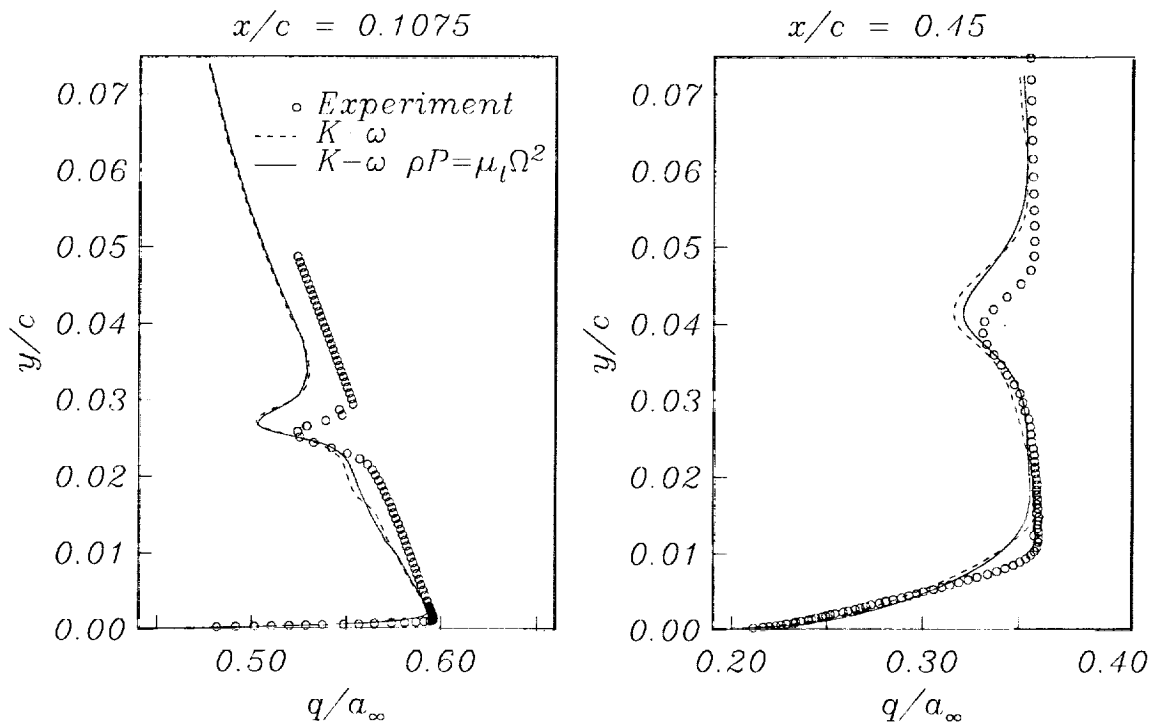


Figure 7: Velocity profiles on the MD-30P/30N main element calculated with alternate production term in the  $K-\omega$  model.

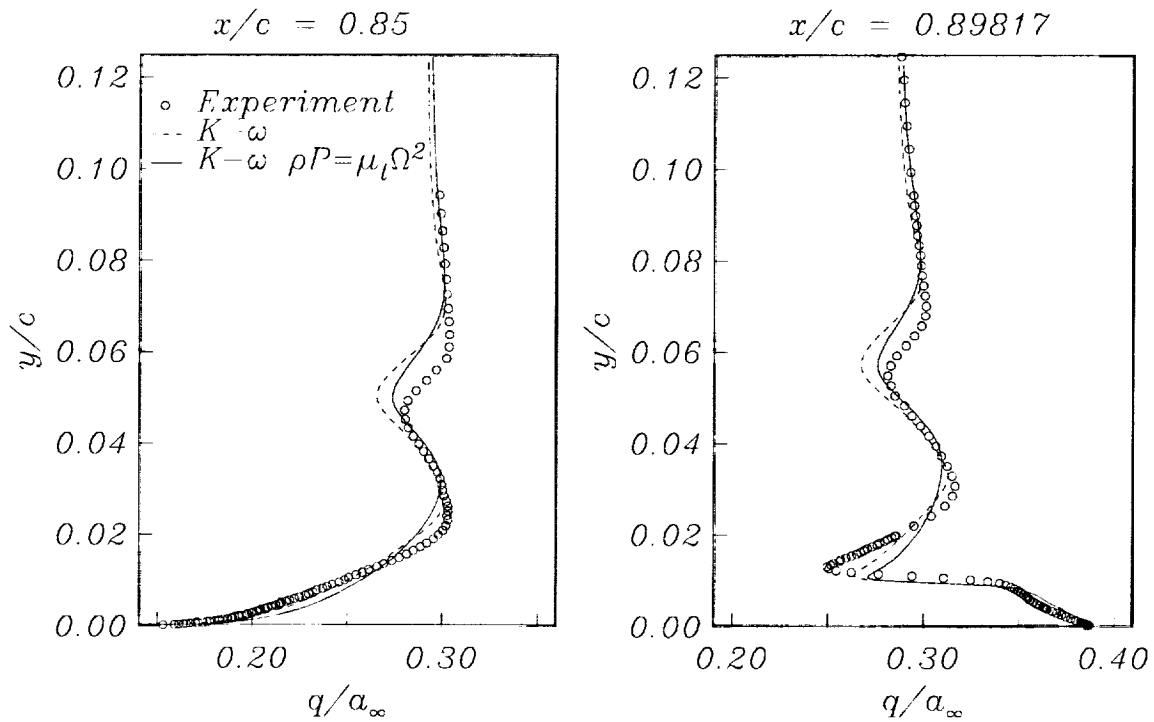


Figure 8: Velocity profiles at the MD-30P/30N main element-flap gap calculated with alternate production term in the  $K-\omega$  model.

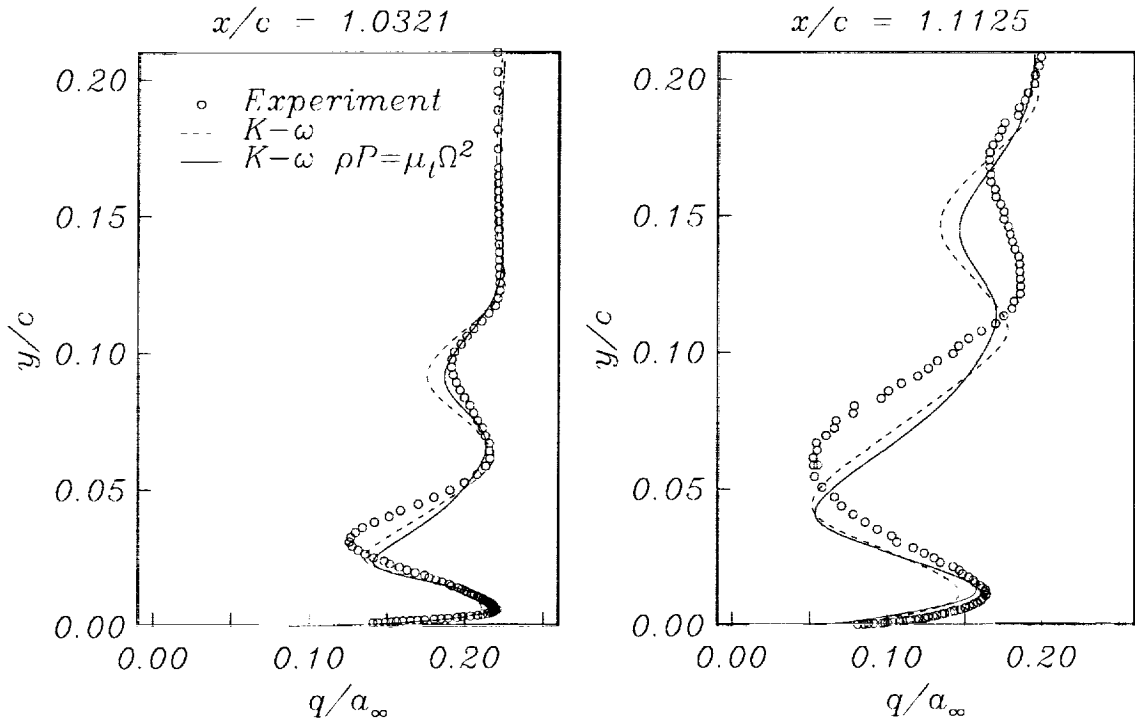


Figure 9: Velocity profiles on the MD-30P/30N flap calculated with alternate production term in the  $K-\omega$  model.

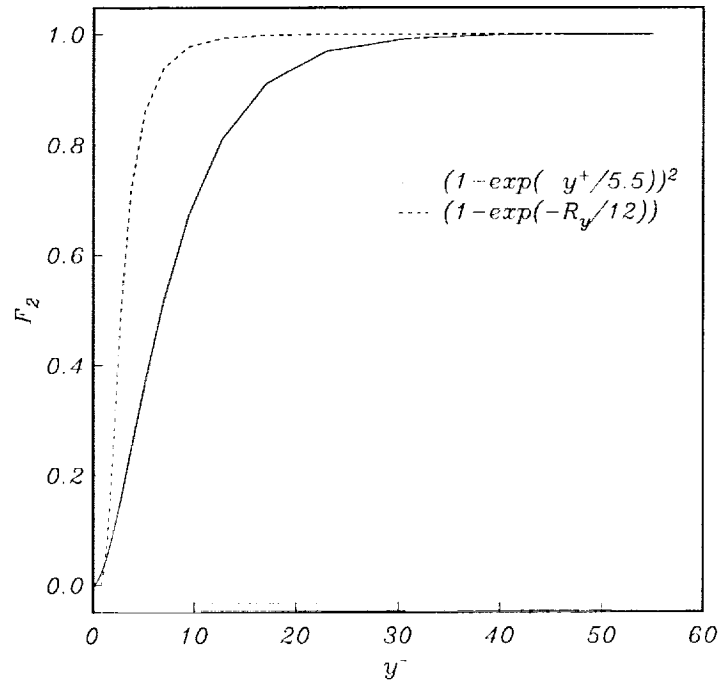


Figure 10: Damping function for ASM and CFL3D ASM models.

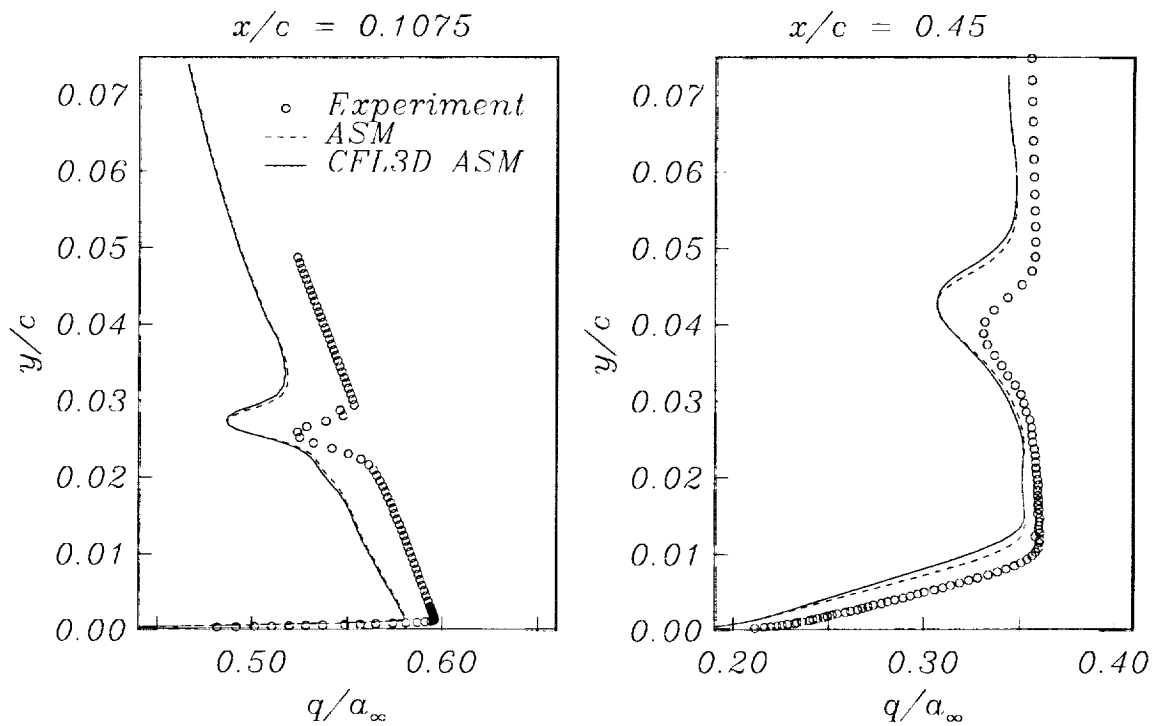


Figure 11: Velocity profiles on the MD-30P/30N main element calculated with ASM and CFL3D ASM models.

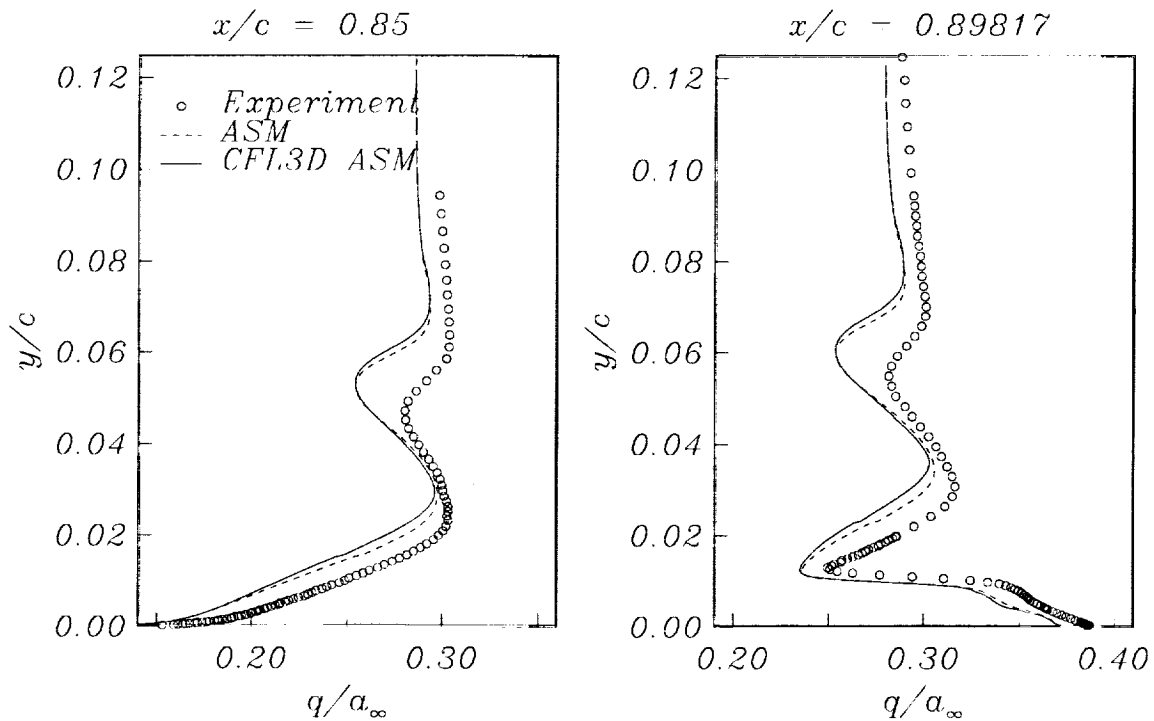


Figure 12: Velocity profiles at the MD-30P/30N main element-flap gap calculated with ASM and CFL3D ASM models.

**Figures**

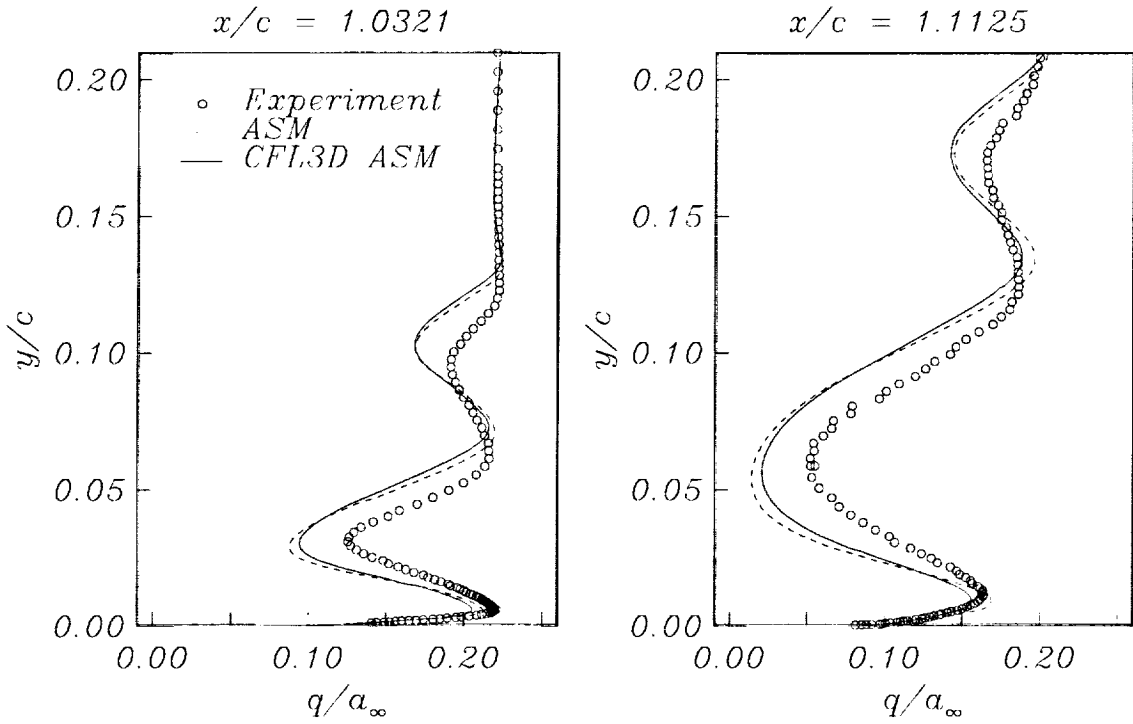


Figure 13: Velocity profiles on the MD-30P/30N flap calculated with ASM and CFL3D ASM models.

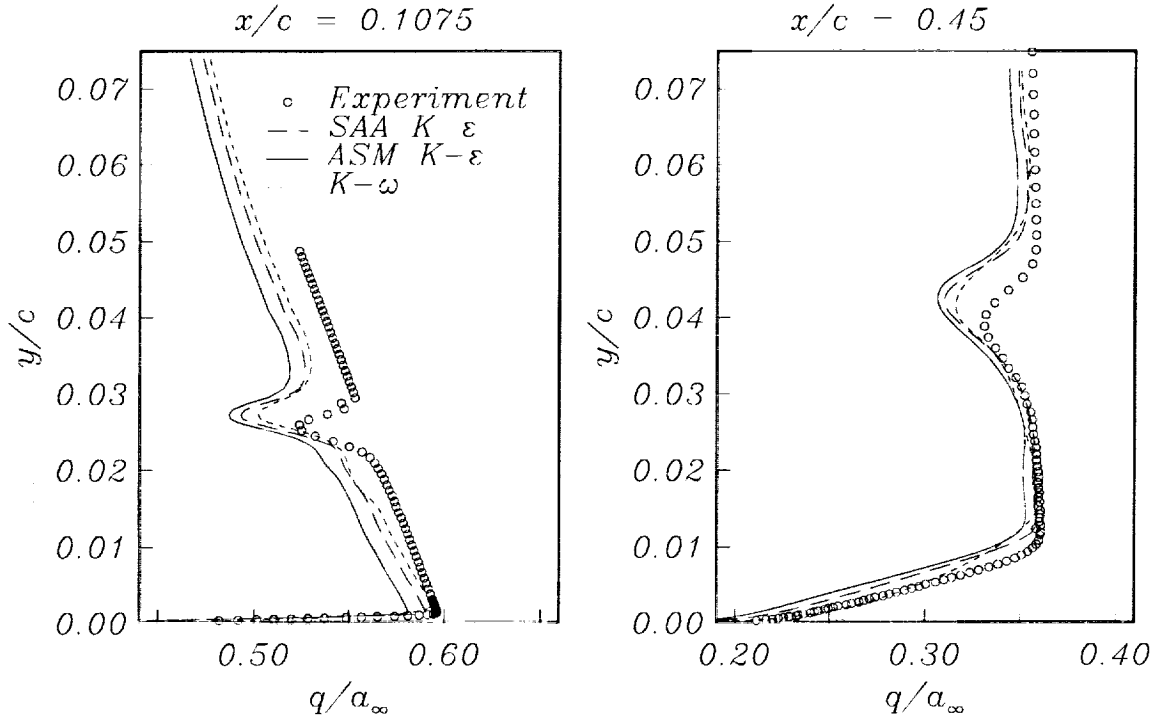


Figure 14: Velocity profiles on the MD-30P/30N main element calculated with  $K-\epsilon$ , ASM, and  $K-\omega$  models.

Figures

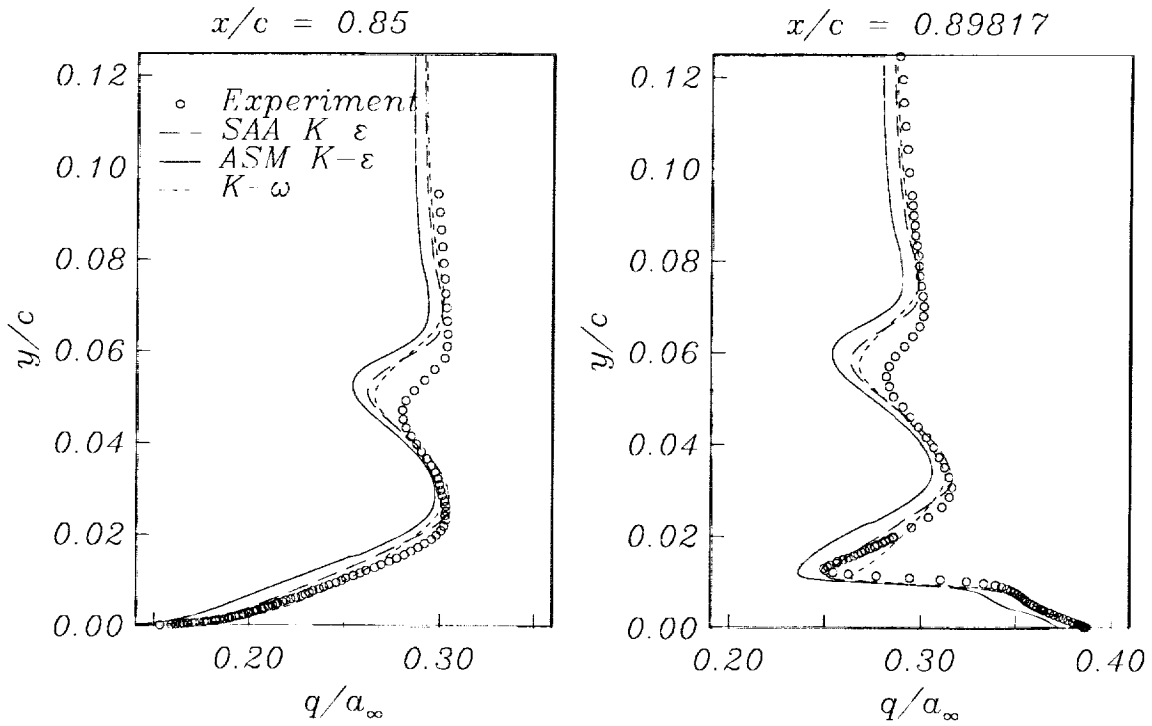


Figure 15: Velocity profiles at the MD-30P/30N main element-flap gap calculated with  $K-\epsilon$ , ASM, and  $K-\omega$  models.

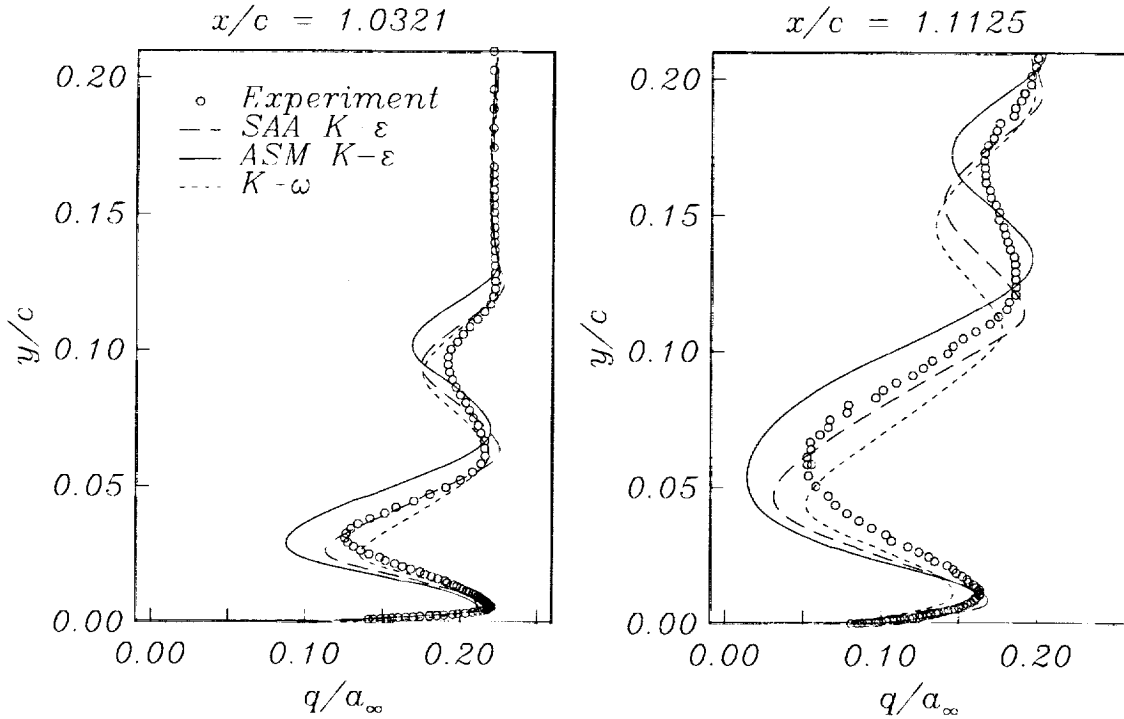


Figure 16: Velocity profiles on the MD-30P/30N flap calculated with  $K-\epsilon$ , ASM, and  $K-\omega$  models.

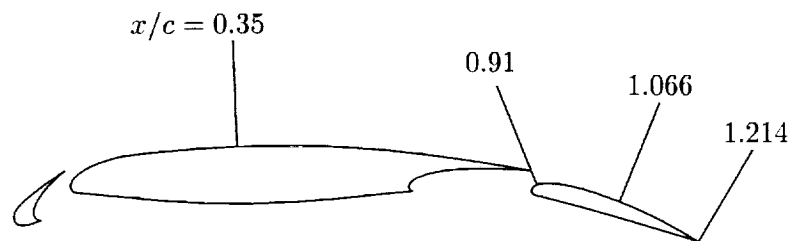


Figure 17: Location of total pressure profiles for NHLP-2D three element airfoil.

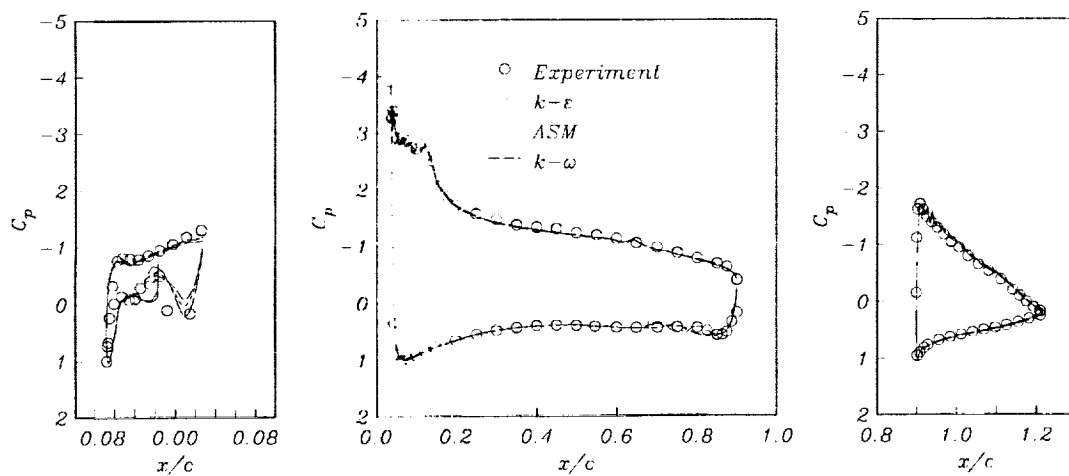


Figure 18: Wall pressure coefficient for NHLP-2D three element airfoil calculated with free transition on the slat and flap.

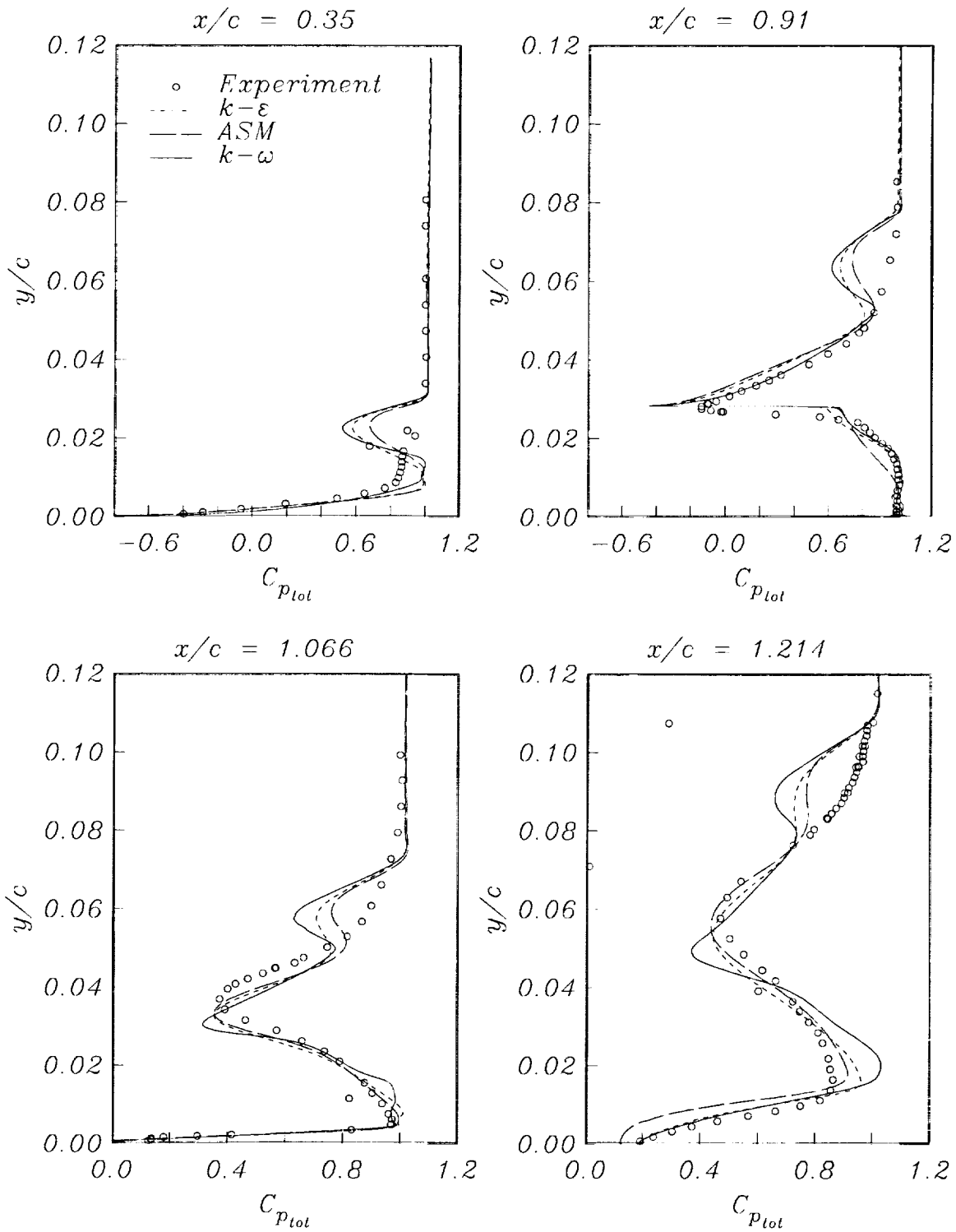


Figure 19: Total pressure coefficient profiles for the NHLP-2D three element airfoil calculated with free transition on the slat and flap.

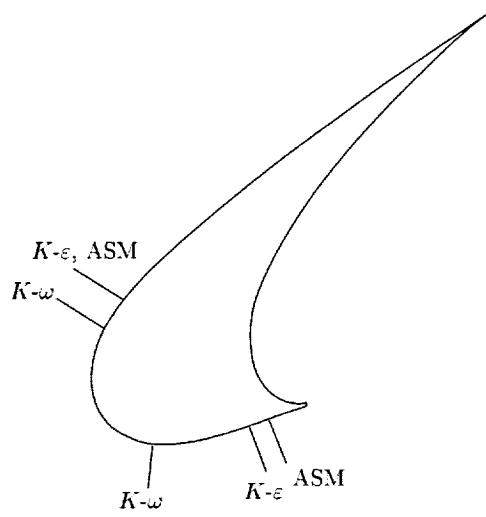


Figure 20: Turbulence model transition locations for the NHLP-2D slat.

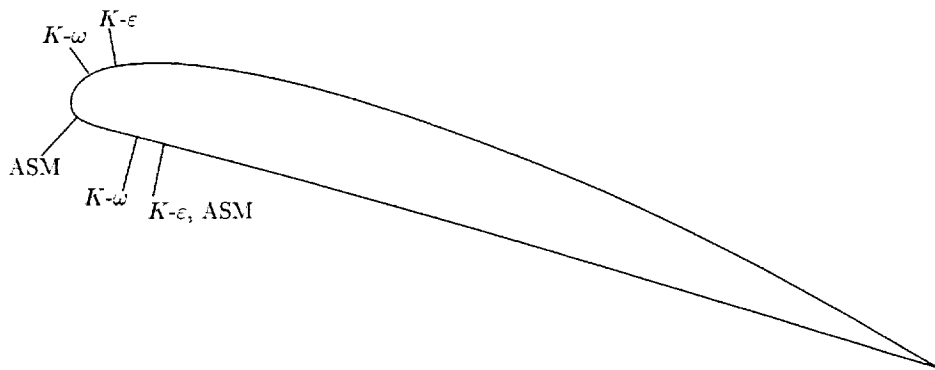


Figure 21: Turbulence model transition locations for the NHLP-2D flap.

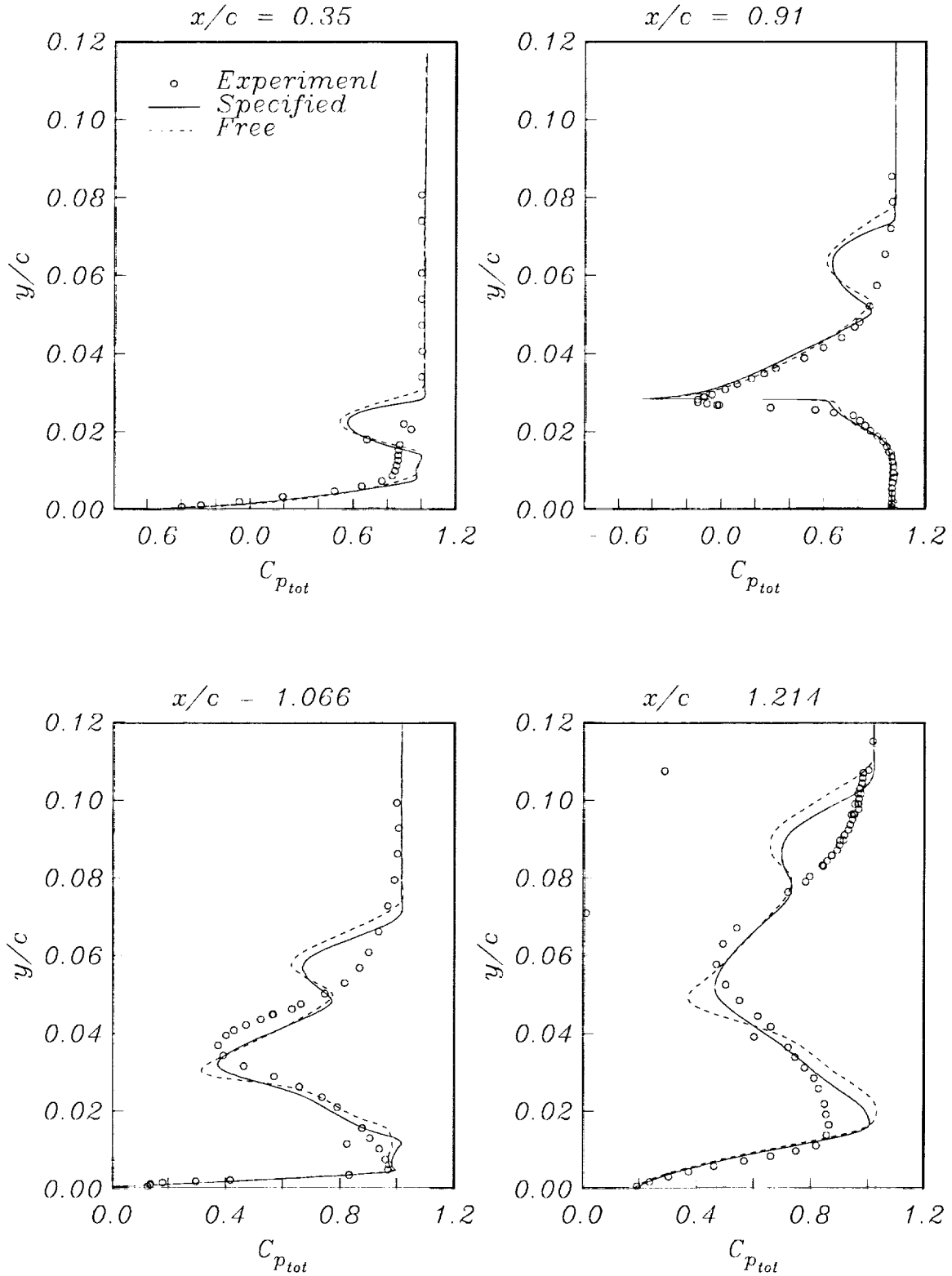


Figure 22: Total pressure coefficient profiles for the NHLP-2D three element airfoil calculated with the  $K-\omega$  model with free and specified transition on the slat.

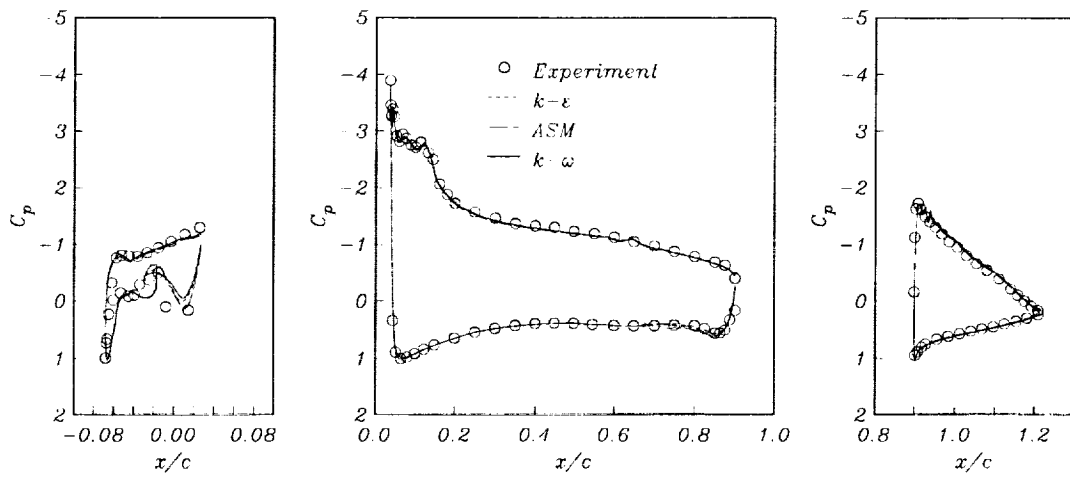


Figure 23: Wall pressure coefficient for NHLP-2D three element airfoil calculated with specified transition on the slat.

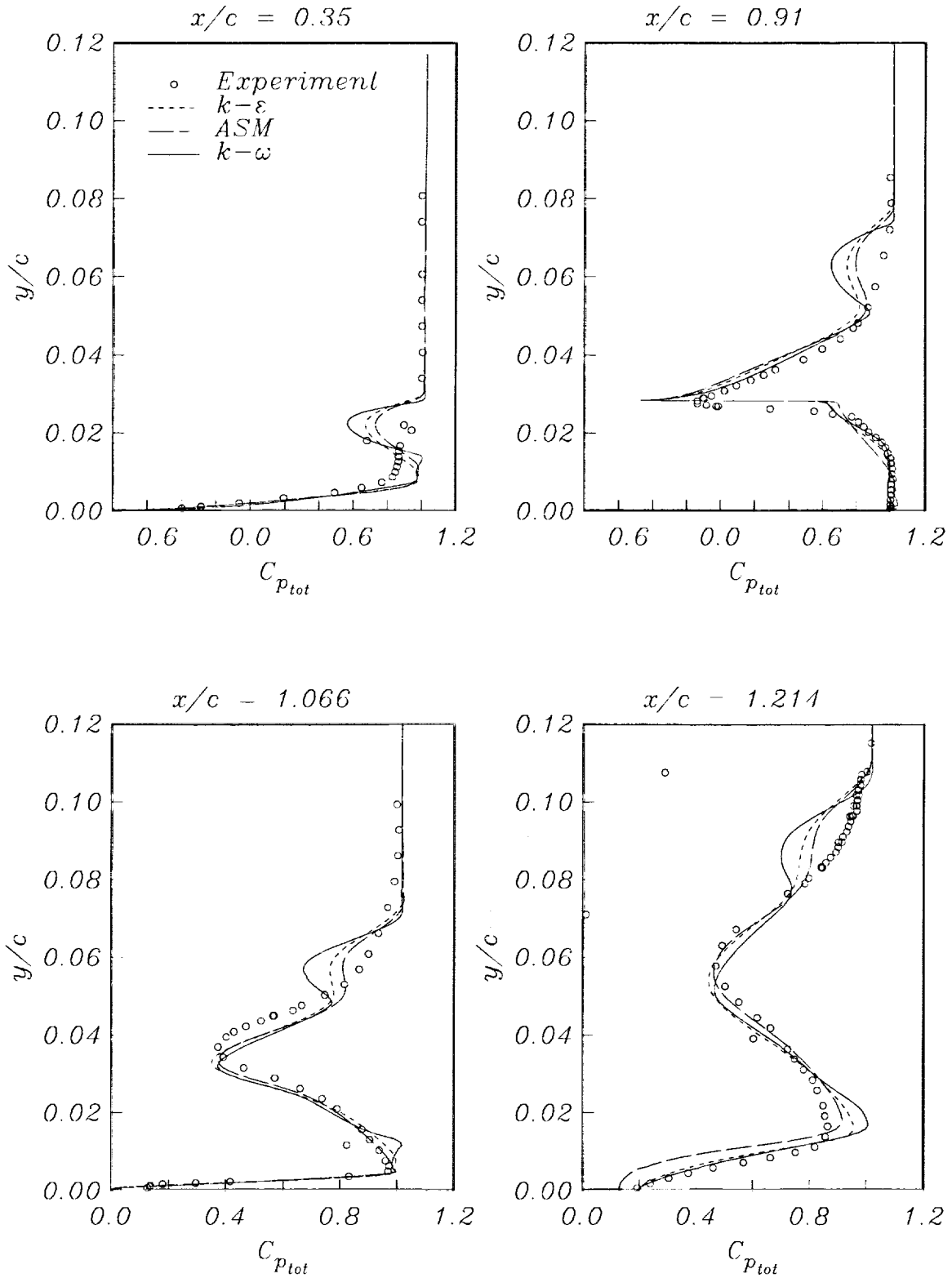


Figure 24: Total pressure coefficient profiles for the NHLP-2D three element airfoil calculated with specified transition on the slat.

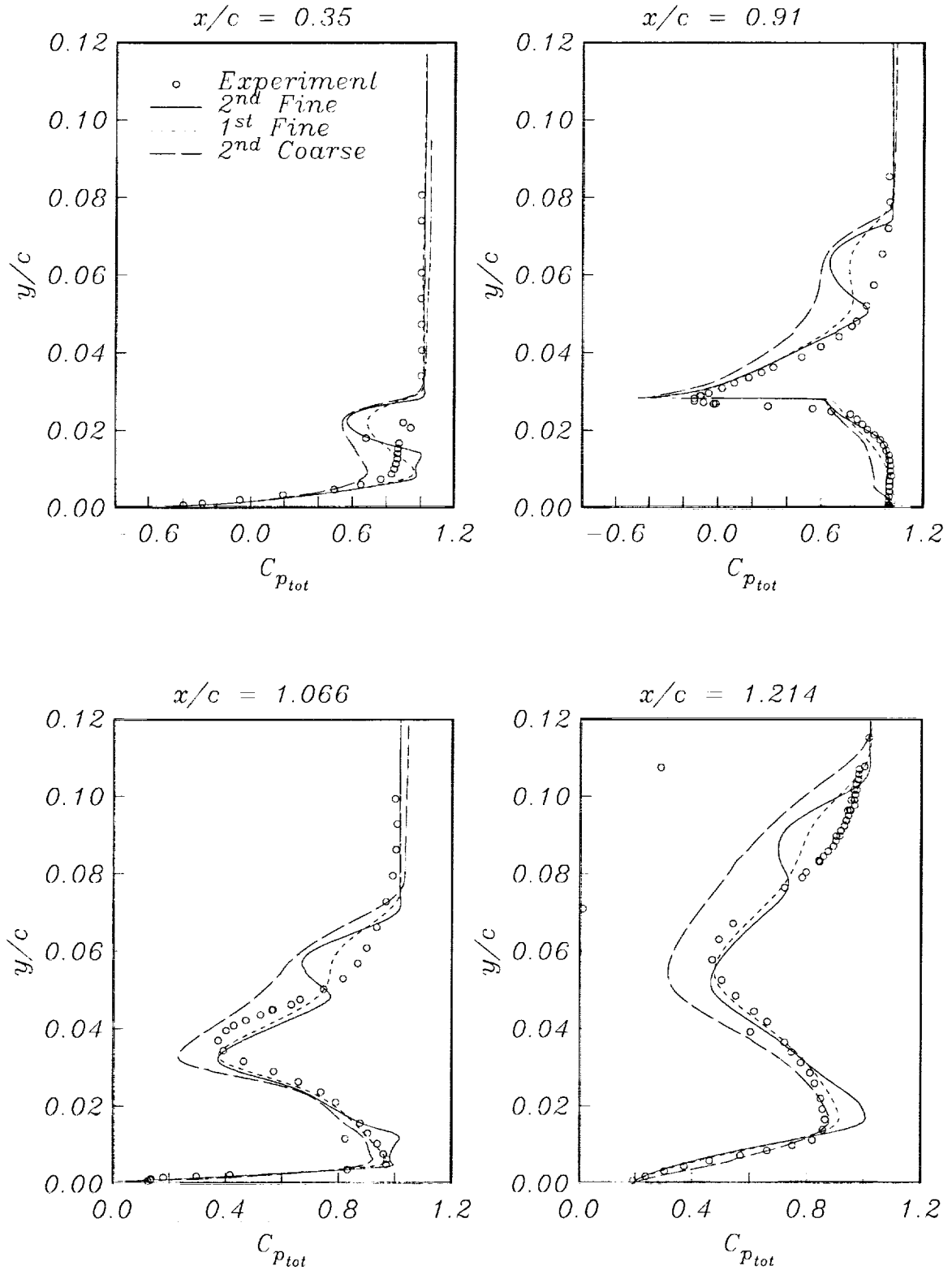


Figure 25: The effect of first vs. second order accurate advection terms for the turbulence equations of the  $K-\omega$  model on the NHLP-2D airfoil.

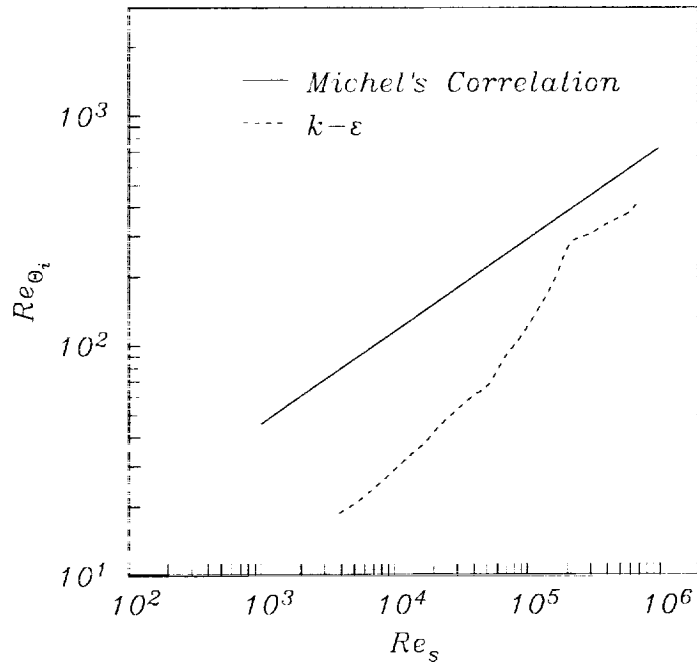


Figure 26: Slat transition predicted with Michel's correlation.

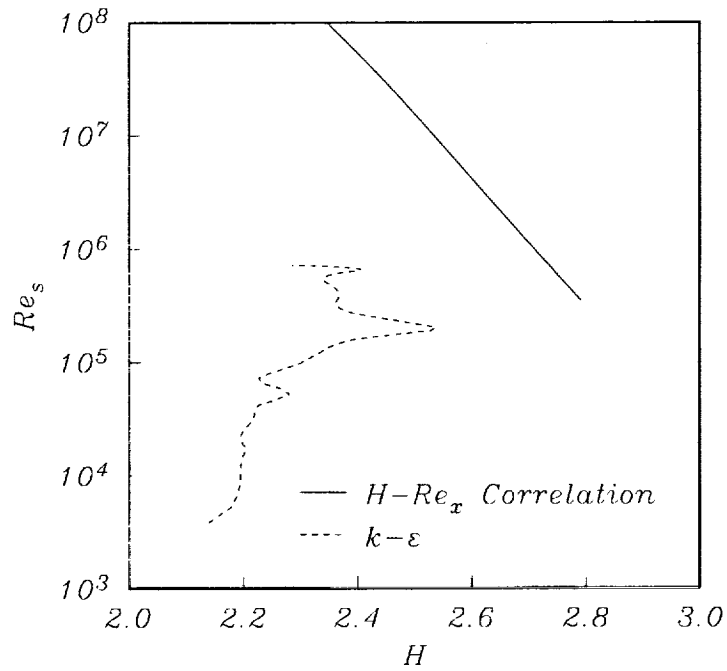


Figure 27: Slat transition predicted with the  $H-Re_x$  method of Wazzan et al.

